The Lorenz Energy Cycle of the Southern Ocean Mode
- Master Thesis -

André Jüling
Supervisors: Henk A. Dijkstra and Jan P. Viebahn

September 2014

Current climate models employ horizontal grid resolutions of about 1° in the ocean component which do not allow for the explicit representation of mesoscale processes such as eddies. It is likely that this limitation implies an underestimation of the variability of crucial climate quantities (e.g. the global mean temperature) since eddy-resolving ocean models enable specific modes of internal low-frequency variability that are not excited in non-eddy-resolving ocean models. Recently, the emergence of the so-called Southern Ocean Mode (SOM) in a state-of-the-art global eddy-resolving ocean model was described. The SOM exhibits multidecadal variability in the global ocean heat content of intense magnitude and appears to originate from interlinked dynamics of the Antarctic Circumpolar Current and neighboring gyres. In this study we continue the analysis of the SOM by exploring, for the first time, the time evolution of the mechanical energy cycle (the Lorenz energy cycle, LEC) in a realistic global eddy-resolving ocean model. We show that all globally integrated components of the LEC, that is, generation, reservoir, and conversion terms, exhibit multidecadal variability on the time scale of the SOM. The mechanical energy analysis yields further insights into the complexity of the large-scale internal ocean variability related to the SOM where several processes such as baroclinic and barotropic instabilities and mean-eddy-topography interactions turn out to be crucial.

1 Introduction

Energy is a fundamental concept of physics and the first law of thermodynamics, the conservation of energy, is a powerful framework in which a system can be analyzed. The energetic viewpoint offers an elementary way of investigating the climate and the ocean in particular.

The energetics of the ocean can be partitioned into four energy types.

1. Kinetic energy
2. Gravitational potential energy
3. Internal/thermal energy
4. Chemical potential

Of these, kinetic energy is especially intuitive as it relates to the movement of the water masses. Together with the gravitational potential energy, relating the vertical positioning of the water masses, it comprises the mechanical energy of the ocean. The internal energy is determined by the temperature distribution and the total is the ocean heat content. The chemical potential, arising from the heterogeneous distribution of chemicals, is sometimes incorporated into the internal energy. Both potential and kinetic energy plus their generation, conversions, and dissipation, make up the mechanical energy or Lorenz energy cycle (LEC).

However, our understanding of the ocean's energetics is still limited. Because there is no equivalent to the equation of motion for the density, as it depends on temperature, salinity and pressure through a nonlinear equation of state, the potential energy terms are not easy to diagnose. Furthermore, eddy resolving ocean model are becoming available only now, too many processes had to

be parameterized before which made the models energetically inconsistent (Eden et al., 2014).

In the ocean, energy is predominantly exchanged at the interface with the atmosphere while different energy forms can be converted into one another in the interior. Mechanical energy is exchanged via momentum transfer and buoyancy fluxes. The change in the ocean heat content (OHC) is mainly determined by sensible and latent heat fluxes as well as radiative fluxes. The geothermal heat flux at the bottom of the ocean is small, may however be important for the abyssal circulation (Huang, 2004). In the employed model, there is no direct conversion between OHC and LEC, for example through frictional dissipation, but dynamically they are coupled. The temperature distribution directly affects the potential energy distribution through the density while heat is advected by currents.

Mechanical energy fluxes are much smaller than thermal energy fluxes in the ocean, yet the mechanical energy input drives the ocean circulation (Huang, 2004) because the ocean is heated at the top only (Sandström, 1908). This is contrast to the atmosphere which converts differential heating, i.e. thermal energy, into mechanical energy. The ocean is thus said to behave as a wind mill while the atmosphere acts as a heat engine.

It is important to understand the energetics of the ocean both to explain current and past behaviour and anticipate future changes. One major motive is to understand the role of the ocean as the largest heat reservoir in the climate system. Currently, the ocean takes up 94 % of the additional heat trapped by anthropogenically added greenhouse gases (Johnson and Parsons, 2015, Fig. 3.7).

The global mean surface temperature (GMST) is arguably one the most important indices of the climate. In equilibrium, the GMST results from the need for the incoming shortwave solar radiation to be balanced by outgoing longwave radiation. However, transiently, the ocean heat uptake is crucial to determining the response of the GMST to a forcing (Schwartz, 2007).

The link between the ocean heat uptake and the dynamics is currently investigated by many studies after the GMST seemed to have risen more slowly following the years after the strong 1998 El Niño.

For example, Kosaka and Xie (2013) fixed the equatorial Pacific SST to observations in an otherwise free-to-evolve coupled climate model and found that this explains an increase in ocean heat uptake. (England et al., 2014) followed up on this and showed that the strength of the Pacific trade winds leads these unusually cold equatorial Pacific SSTs. In line with these finding, Steinman et al. (2015) analyzed the influence of the Atlantic and Pacific Multidecadal Oscillation on the surface temperature of the Northern hemisphere and found the Pacific to contribute strongly negatively at the moment and the Atlantic slightly positively.

The idea of the hiatus is currently being rescinded after observations were recalibrated (Karl et al., 2015). Nonetheless, it is still of great interest to understand the dynamics of ocean heat uptake and how it relates to the mechanical energy budget. Because, on a more abstract level, any multidecadal variability in the GMST must be related to the heat budget of the ocean, as it is not observed in the radiative forcing (Hansen et al., 2011).

This study explores the time dependent mechanical energy budget of a high resolution ocean model. The coupling between OHC and the mechanical energy is investigated because multidecadal variability in the OHC is observed (Le Bars et al., 2015, in review). The use of a high resolution model is crucial as only eddy permitting models exhibit the multidecadal variability.

The following section introduces the Southern Ocean Mode found by Le Bars et al. (2015). Next, the concept of the mechanical energy cycle in the climate system and the ocean in particular is introduced before the Parallel Ocean Program is described. Subsequently, the results are presented and are then discussed. Finally, in the last section conclusions are drawn.

2 Southern Ocean Mode

A previously unknown mode of internal multidecadal variability was found by Le Bars et al. (2015, in review). The mode is located in the Southern Ocean and has a period of 40-50 years. It is designated the Southern Ocean Mode (SOM).

The employed high resolution ocean only model resolved the internal Rossby radius of deformation and thus permitted meso-scale eddy processes. These appear crucial for the mode to develop as a low resolution version of the model did not exhibit the mode.

The SOM can be observed in the sea surface temperature (SST), the surface heat flux (SHF), and the OHC and is localized in the South Atlantic, the

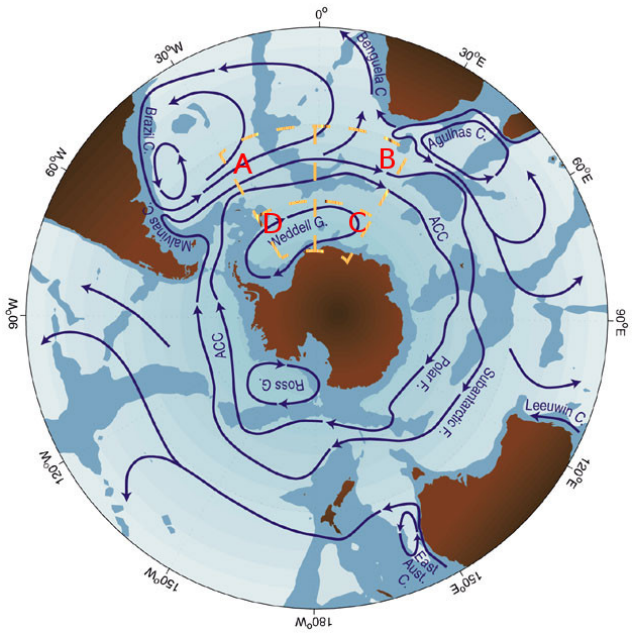

Figure 1: An overview of the ocean currents of the Southern Hemisphere. Shaded areas are shallower than 3500 m, while C, F, and G mark currents, fronts and gyres, respectively. SOM regions A-D are marked with yellow dashed lines. Adapted from (Rintoul et al., 2001).

Antarctic Circumpolar Current (ACC) between the Drake Passage and South Africa as well as the Weddell Gyre (see Fig. 1). The peak to peak variability in the OHC is significant with 60 ZJ. For comparison, between 1970 and 2010 the ocean gained 250 ZJ of heat of which 170 ZJ was gained in the upper 700 m (IPCC WGI, 2014).

As there is only a sparse and short observational record of temperature data in this region, the SOM has not been detected in the climate system yet. This demonstrates the necessity for continued and improved observations especially in the Southern Ocean.

For the analysis in this paper, four index regions are defined - SOM-A, B, C, and D. They are arranged clockwise starting in the North-Western corner in $[30\,°\mathrm{W}, 30\,°\mathrm{E}] \times [70\,°\mathrm{S}, 40\,°\mathrm{S}]$. These regions are plotted in Fig. 1 and their geographic details can be found in Table 1.

A SOM index is defined as the difference in OHC of the Northern region, SOM-AB, and the Southern region, SOM-CD.

$$\mathrm{SOM} := \mathrm{OHC(SOM\text{-}AB)} - \mathrm{OHC(SOM\text{-}CD)} \quad (1)$$

When the SOM index is positive (negative), the SOM is in a warm (cold) phase. The global OHC is lowest in the warm SOM phase (Fig. 2).

Table 1: Properties of SOM index regions.

SOM	lon.	lat.	area	volume
-	[°E]	[°S]	$[10^6\,\mathrm{km}^2]$	$[10^6\,\mathrm{km}^3]$
A	$[-30, 0]$	$[40, 58]$	4.40	16.4
B	$[0, 30]$	$[40, 58]$	4.40	18.6
C	$[-30, 0]$	$[58, 70]$	1.95	8.51
D	$[0, 30]$	$[58, 70]$	1.95	8.81

Figure 4 shows oscillations of the SST, SHF, and OHC in SOM-A and SOM-D with phase shifts of approximately 0, 90, and 180 degrees, respectively. Once excited, the thermal oscillations can be explained with the anti-correlation of the SHF and the SST because of the radiative feedback (implemented as a restoring heat flux) as well as the dependency of the SST on the OHC. The OHc follows the SHF because at maximum SHF anomaly the OHC anomaly grows most and will continue to grow as long as the SHF exhibits a positive anomaly. A high (low) OHC leads to an increase (decrease) in SST which reaches its maximum (minimum) only after the OHC.

The oscillation appear first in AB then in CD which indicates that they are initiated in the Northern region.

The horizontal evolution of the vertically integrated OHC through a 50 year SOM cycle can be seen in Fig. 3 as decadal anomalies.

Starting in SOM-A, the temperature anomalies are advected East with ACC with a velocity of about $0.01\,\mathrm{m\,s}^{-1}$. The anomalies propagate smoothly in the South Atlantic until, South of Africa, the Agoulhas retroflection interrupts this transport. Part of the anomaly is transported into the Indian ocean and appears to dissipate there South of 50 °S. The other part is advected South due to enhanced meridional eddy fluxes (Sallée et al., 2008) where it enters the Weddell Gyre. The Weddell Gyre returns the anomalies back to the South Atlantic East of the Drake Passage. There they propagate almost adiabatically down the steep isopycnals against the Ekman upwelling. This is happens through strong along-isopycnal eddy diffusion.

Through the relative change in OHC between SOM-AB and SOM-CD, the meridional density gradient changes. This impacts the shear of the zonal velocity via the thermal wind balance:

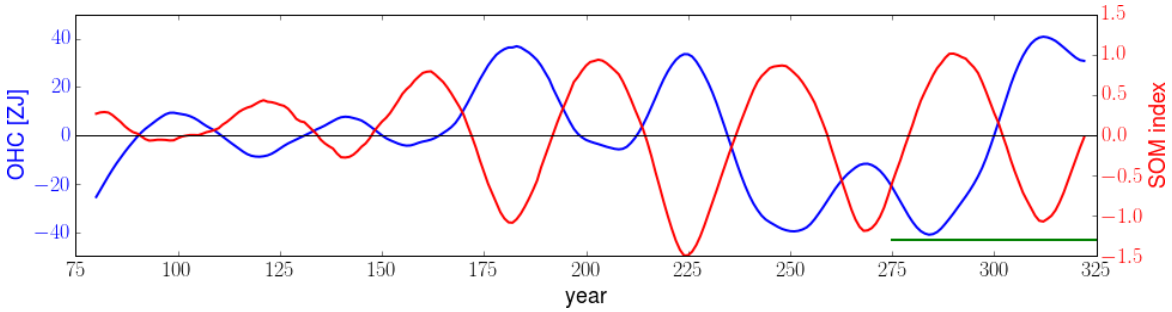

Figure 2: Quadratically detrended OHC (blue) and SOM index (red) over the all model years 75-325. The green line visualizes the time with full model output analyzed in this study.

$$f_0 \frac{\partial u}{\partial z} = \frac{g}{\rho_0} \frac{\partial \rho}{\partial y} \tag{2}$$

This change in the vertical shear of the zonal velocity affects the ACC transport. A stronger (weaker) meridional density gradient during the warm (cold) phase results in a stronger (weaker) ACC transport as can be seen in Figure 4.

Part of the OHC anomaly is advected meridionally into the North Atlantic where it affects the Atlantic Meridional Overturning Circulation (AMOC). As there is no southward advection of an anomaly, Le Bars et al. (2015) conclude that the AMOC only reacts to the SOM and does not initiate it.

It is unclear how the SOM would impact the fully coupled climate system because it has only been observed in an ocean only model. This restricted setup entails strong assumptions, such as an infinite heat capacity of the atmosphere. Any feedbacks, for example with the atmospheric surface temperature and hence the top of the atmosphere radiative imbalance, are omitted. In the least, the SOM indicates that one can expect additional modes of variability in earth system models once eddies are resolved.

This study extends the time series of Le Bars et al. (2015) by 51 years. The SOM continues for another cycle but does not grow in amplitude.

3 Lorenz Energy Cycle

The mechanical energy of the atmosphere comprising kinetic and potential energy was first described by Lorenz (1955). Similarly, potential and kinetic energy can be analyzed in the ocean. These energies are generated through surface processes and can be converted into one another in the ocean interior. In the steady state, energy generation equals dissipation so that the size of the energy reservoirs do not change. The mechanical energy cycle is called the Lorenz energy cycle (LEC) in honor of Edward N. Lorenz.

As the total potential energy can never be converted, Lorenz (1955) introduced the concept of available potential energy (APE) which denotes the energy that is accessible for conversion/dissipation. The APE is the difference between the potential energy of a state and an adiabatically redistributed, minimal potential energy ground state of the same water masses. Calculating this ground state is not trivial in the case of complex bathymetry as basins can be isolated from one another.

Eulerian mean decomposition of the total into a mean and eddy part can be applied to differentiate mean and eddy components of the LEC. The mean is the average over a suitable time span, while the eddy part is the perturbations from that average:

$$\overline{xy} = \bar{x}\bar{y} + \overline{x'y'} \tag{3}$$

where the bar denotes an average in time. This relationship is computationally convenient as both the individual quantities, $\bar{x}$ and $\bar{y}$, and their product, $\overline{xy}$, can easily be written out from a numerical model. Subsequently, mean and eddy components are indicated by the subscripts m and e (for calculated quantities) or a bar ($\bar{x}$) and a dash (x') (for output variables), respectively. Kinetic energy and APE reservoirs are symbolized by K and P.

To write out single equations that hold for all energy reservoirs, the dummy reservoirs X and Y are introduced. Furthermore, the generation of X is denoted $G(X)$ while conversion from X to Y and

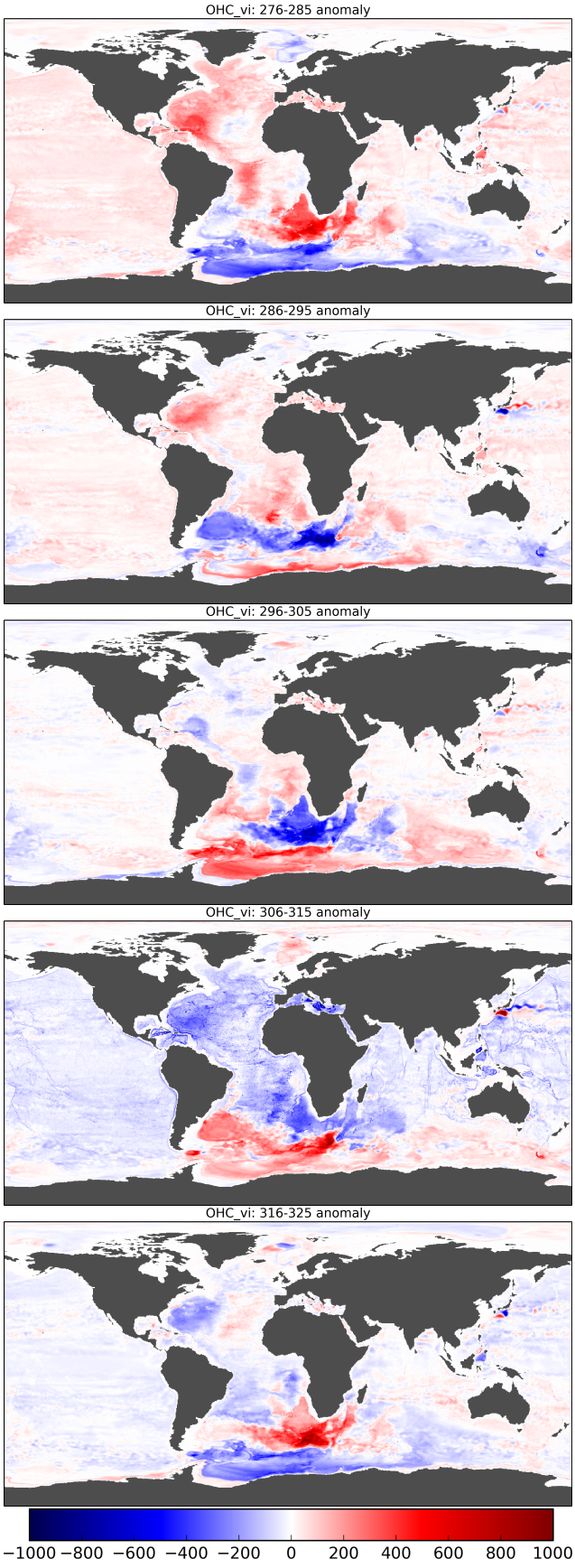

Figure 3: Evolution of the vertically integrated OHC anomalies in the cycle 276-325. No detrending has been done which explains the apparent global cooling. The 50 year mean was subtracted from decadal averages. Units are $\mathrm{J\,m^{-2}}$.

dissipation of X are is denoted by $C(X,Y)$ and $D(X)$.

In all calculations the potential density is used to circumvent problems with compressive effects.

The following subsections introduce the different terms of the LEC.

3.1 Reservoirs

As a ground state for the calculation of the APE, von Storch et al. (2012) used the area average of the potential density ρ in each model layer and denoted it

$$\rho_{ref}(z,t) = \langle\overline{\rho(x,y,z,t)}\rangle \tag{4}$$

where the angled brackets indicate an area mean while the bar denotes an approbriate time average, in the present case a one year average. The resulting density profile $\rho_{ref}(z)$ is positively stratified. Density anomalies are defined as the departure from this reference density:

$$\rho^*(x,y,z) = \rho(x,y,z) - \rho_{ref}(z) \tag{5}$$

The mean and eddy APE reservoirs are calculated with

$$P_m = -\frac{g}{2}\int_V \frac{1}{n_0}\bar{\rho}^{*2}\,\mathrm{d}V \tag{6a}$$

$$P_e = -\frac{g}{2}\int_V \frac{1}{n_0}\overline{\rho^{*\prime 2}}\,\mathrm{d}V \tag{6b}$$

where $g = 9.81\,\mathrm{m\,s^{-2}}$ is the gravitational acceleration, $n_0(z)$ is the vertical gradient of the time and area mean of the potential density, and $\mathrm{d}V$ denotes the volume integral over the whole ocean. The density terms can be rewritten in the following way: $\bar{\rho}^{*2} = (\bar{\rho} - \rho_{ref})^2$ and $\overline{\rho^{*\prime 2}} = \overline{(\rho - \rho_{ref})^{\prime 2}} = \overline{(\rho - \rho_{ref})^2} - \overline{(\rho - \rho_{ref})}^2 = \overline{\rho^2} - \bar{\rho}^2$.

Much like the total of the OHC, the size of the P reservoirs is relatively meaningless because of an arbitrary reference level. Only from the change conclusions can be drawn.

The kinetic energy reservoirs can be computed as:

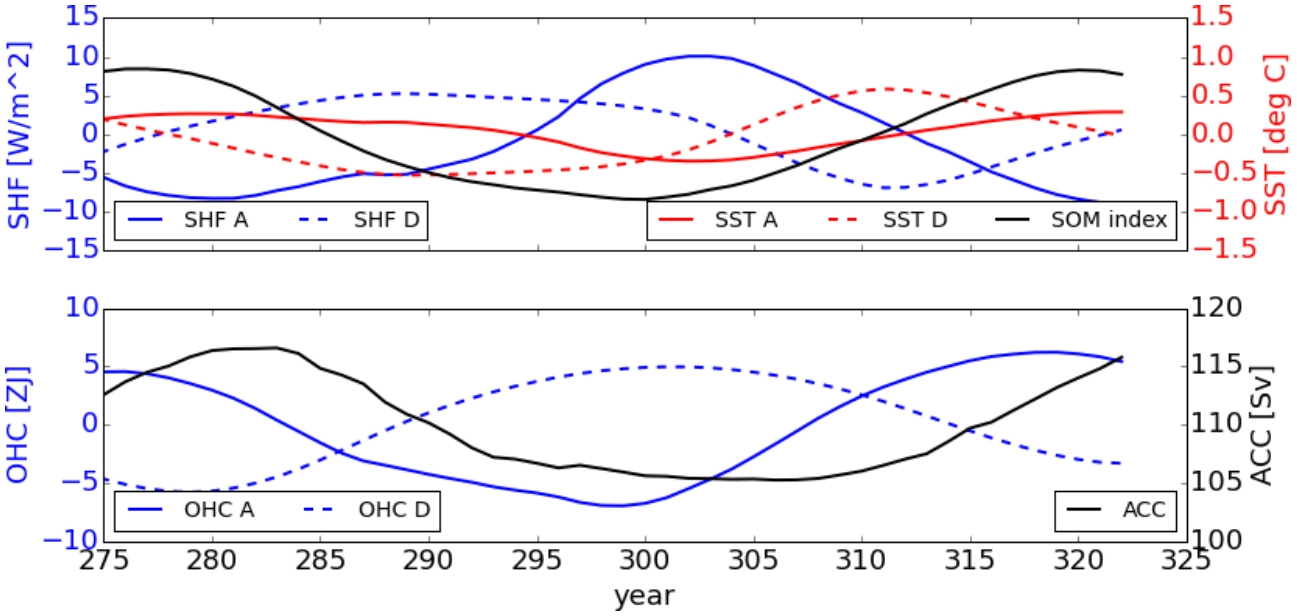

Figure 4: Signals of the SOM in region A (solid lines) and D (dashed). The top panel shows the surface heat flux anomalies (blue) and the anticorrelated SST (red) while the lower panel shows the signal in the OHC of the respective regions. Furthermore, the SOM index and the ACC transport are displayed in the upper and lower figures as black solid lines.

$$K_m = \frac{\rho_0}{2} \int_V \left(\bar{u}^2 + \bar{v}^2\right) \mathrm{d}V \tag{6c}$$

$$K_e = \frac{\rho_0}{2} \int_V \left(\overline{u'^2 + v'^2}\right) \mathrm{d}V \tag{6d}$$

where the x-component of the K_e-term is $\overline{u'^2} = \overline{u^2} - \bar{u}^2$ as per Eulerian mean decomposition. The density $\rho_0 = 1026\,\mathrm{kg\,m^{-3}}$ is the global average density of sea water.

3.2 Generation

Because mechanical energy is lost to the ocean as a systems, e.g. through frictional dissipation, there need to be sources of energy to maintain the general circulation of the ocean. Potential and kinetic energy are created at the surface of the ocean through buoyancy fluxes and wind stresses, respectively.

Buoyancy fluxes are composed of heat fluxes (sensible and latent heat as well as radiative fluxes) and freshwater/salinity fluxes (evaporation, precipitation, and river runoff).

$$G(P_m) = -g \int_S \left(\underbrace{\frac{\alpha_{0,1}}{n_0} \overline{J_s \rho^*}}_{\text{heat}} + \underbrace{\frac{\beta_{0,1}}{n_0} \overline{G_s \rho^*}}_{\text{salinity}} \right) \mathrm{d}S \tag{7a}$$

$$G(P_e) = -g \int_S \left(\underbrace{\frac{\alpha_{0,1}}{n_0} \overline{J'_s \rho'}}_{\text{heat}} + \underbrace{\frac{\beta_{0,1}}{n_0} \overline{G'_s \rho'}}_{\text{salinity}} \right) \mathrm{d}S \tag{7b}$$

where $\alpha_{0,1}$ and $\beta_{0,1}$ are expansion coefficients in the upper most model layer, J_s and G_s are temperature and salinity fluxes at the surface. These fluxes can be computed via $J_s = H/\rho_s c$ and $G_s = \bar{S}_1(E-P)$, where H is the total heat flux, $c = 4000\,\mathrm{J\,kg^{-1}\,K^{-1}}$ the specific heat of sea water, $\bar{S}_1$ the time-mean surface salinity, and $(E-P)$ the difference between evaporation and precipitation. The integral $\int \mathrm{d}S$ is taken over the whole surface of the ocean.

Some terms can be further developed: $\overline{J_s \rho^*} = \overline{J_s(\rho - \rho_{ref})} = \overline{J_s}\,(\bar{\rho} - \rho_{ref})$ and $\overline{J'_s \rho'} = \overline{J_s \rho^*} - \overline{J_s}\,\overline{\rho^*} = \overline{J_s \rho} - \overline{J_s}\,\bar{\rho}$ and equivalently for the salinity terms, $\overline{G_s \rho^*}$ and $\overline{G'_s \rho'}$.

On the other hand, kinetic energy is generated by the wind exerting a stress on the water surface and hence transferring momentum to the water.

$$G(K_m) = \int_S \left(\overline{\tau_x}\bar{u} + \overline{\tau_y}\bar{v}\right) \mathrm{d}S \tag{7c}$$

$$G(K_e) = \int_S \left(\overline{\tau_x' u'} + \overline{\tau_y' v'}\right) \mathrm{d}S \tag{7d}$$

with τ being the wind stress. Again, e.g. the x-component can be decomposed: $\overline{\tau_{x,s}' u'} = \overline{\tau_{x,s}\bar{u}} - \overline{\tau_{x,s}}\bar{u}$.

All four globally integrated generation terms are net positive, i.e. more energy is generated than dissipated through each of these surface processes. However, locally, all of these terms can contribute negatively as well.

3.3 Conversion

There are four conversion pathways between the energy reservoirs. The reverse conversion is simply the opposite, $C(Y, X) = -C(X, Y)$.

The conversion from eddy to mean APE is:

$$C(P_e, P_m) = -\int_V \frac{g}{n_0} \overline{\rho' u_h'} \cdot \nabla_h \bar{\rho} \, \mathrm{d}V \tag{8a}$$

where the subscript h indicates the horizontal components. The x-component, for example, can be expressed as: $\overline{\rho' u'} \partial_x \bar{\rho} = \left(\overline{\rho u} - \bar{\rho}\bar{u}\right) \partial_x \bar{\rho}$.

The transfer of energy from mean to eddy potential energy is due to baroclinic instability which requires sloped isopycnals. Accordingly, the horizontal gradient of the density can be found in (8a).

The conversion of eddy to mean kinetic energy is:

$$C(K_e, K_m) = \rho_0 \int_V \left(\overline{u'\mathbf{u}'} \cdot \nabla \bar{u} + \overline{v'\mathbf{u}'} \cdot \nabla \bar{v}\right) \mathrm{d}V \tag{8b}$$

where the first term in the integral can be written as $\left(\overline{u'\mathbf{u}'} \cdot \nabla \bar{u}\right) = \left(\overline{u'u'} \cdot \partial_x \bar{u} + \overline{u'v'} \cdot \partial_y \bar{u} + \overline{u'w'} \cdot \partial_z \bar{u}\right)$.

This conversion between mean and eddy kinetic energy is due to barotropic instability, i.e. to horizontal shear. Hence the gradients of the velocity in (8b) components.

And lastly, potential energy can be converted into kinetic energy via vertical movement of water masses:

$$C(P_m, K_m) = -g \int_V \bar{\rho}\bar{w} \, \mathrm{d}V \tag{8c}$$

$$C(P_e, K_e) = -g \int_V \overline{\rho' w'} \, \mathrm{d}V \tag{8d}$$

von Storch et al. (2012) find that the most important pathway from P_m to K_e is through baroclinic instability (0.8 TW). From K_m to K_e mostly through P_m. The total power input is 6.4 TW of which 4 TW is generated by the wind. This is in line with Ferrari and Wunsch (2009) who claim that the majority of power input is through the wind.

3.4 Steady State and Dissipation

If one assumes steady state, the time derivative of the reservoir sizes is zero:

$$\frac{\mathrm{d}X}{\mathrm{d}t} = G(X) + C(Y, X) + D(X) = 0 \tag{9}$$

The dissipation of each energy term can then be calculated as the residual:

$$D(P_m) = G(P_m) + C(P_{e,m}) - C(P, K_m) \tag{10a}$$

$$D(P_e) = G(P_e) - C(P_{e,m}) - C(P, K_e) \tag{10b}$$

$$D(K_m) = G(K_m) + C(K_{e,m}) + C(P, K_m) \tag{10c}$$

$$D(K_e) = G(K_e) - C(K_{e,m}) + C(P, K_e) \tag{10d}$$

where, for brevity, $C(X_e, X_m)$ was shortened to $C(X_{e,m})$ and $C(X_z, Y_z)$ to $C(X, Y_z)$.

However, with the 50 yrs time series, it is possible to determine the change in reservoir size over time, such that $\mathrm{d}X/\mathrm{d}t \neq 0$.

The detailed derivation of the LEC terms can be found in the appendix of von Storch et al. (2012) while Wunsch and Ferrari (2004) wrote an extensive review.

4 Parallel Ocean Program

For this study, the model run of Le Bars et al. (2015) with the Parallel Ocean Program (POP) of the Los Alamos National Laboratory was continued for 51 years. To isolate oceanic processes, the

model was run as an uncoupled, ocean only model with monthly mean forcings.

Previous to this study, the model was run for 275 years of which 75 years was used to spin it up. The years 76-275 were used, amongst others, in Le Bars et al. (2015).

The POP model was set up with a high resolution (0.1 °) Arakawa B-grid. This high resolution (horizontal spatial resolution at the equator is about 10 km) allows for meso-scale eddies to be resolved. These eddies are crucial for the development of internal variability. The grid is tripolar with the North pole split into a pole in North America and Northern Asia. The model uses depth as a vertical coordinate and uses 42 levels of increasing depth of 10 to 250 m. In total, there are $3600 \times 2400 \times 42$ grid points.

The model is forced with monthly mean wind fields, radiation and fresh water fluxes. There is no tide prescribed. Conversely, von Storch et al. (2012) used a reanalysis data set to force their ocean model.

The model was run with the full output for 51 yrs from model year 276 to 326. The full mechanical energy balance is analyzed for this period, while K_m, K_e, and $G(K_m)$ are available for time before as well. The averaging period for the mean part is 1 yr which is shorter than the 10 yrs used by von Storch et al. (2012).

4.1 Numerical Details

All output was saved in single-precision floating-point format. Densities ρ were stored as $\rho - \rho_0$ to increase the information content which would otherwise be significantly decreased because the first 2 digits do not contain additional information.

To assure numerical precision of the global integration, values of the terms on each grid point were added using the Kahan summation algorithm (Kahan, 1965).

A source of systematic errors in the calculation of the conversion terms (8a-8d) may arise from the use of product terms as opposed to flux terms. A flux formulation may improve the estimate of the conversion terms.

4.2 Limitations

The model is of course not a complete representation of the physical oceans as it misses some forcings and processes. For example, there are no tides which eliminates an important source of energy in the real ocean. There is no atmospheric loading generated through varying high and low pressure areas in the atmosphere and there is no geothermal heat flux.

Due to limitations in resolution to 0.1 °, there are missing physical processes such as surface waves. At the far end of the range of scales important in the ocean, molecular mixing can only be parameterized. Furthermore, the internal wave field is neither resolved and nor parameterized. The POP model is not yet set up to be energetically consistent as suggested by Eden et al. (2014).

Processes arising from the nonlinearity of the equation of state, such as salt fingers and cabbeling are also not captured by the model as their scale is too small (Huang, 2004).

5 Results

5.1 Statistics and Localization of LEC

Generally the same horizontal patterns and vertical profiles as in von Storch et al. (2012) have been found in the analysis of the POP model output. For example, the mean kinetic energy at about 100 m in Fig. 6 compares well with Fig. 1a of von Storch et al. (2012). The schematic overview Fig. 5 shows that the sizes of most terms are comparable although the POP model terms are often somewhat larger.

The mean kinetic energy is localized in boundary and equatorial currents (and meso-scale eddies if the averaging period is short enough; see Fig. 6). The eddy kinetic energy is spatially more distributed. Vertically all energy terms reduce with depth (not shown). Both the APE terms show an intensification at depths below 5 km which may be both due to bottom intensified mixing and isolated basins with different densities from one another possibly resulting in large density anomalies ρ^*.

The geographic distribution of the generation terms is mostly determined by the mean atmospheric climate and river outlet locations. Potential energy is mostly generated by heat fluxes with cooling in the downwelling regions of the North Atlantic and along the Antarctic continental shelf contributing most mean potential energy. Eddy APE is mostly generated by cooling East of the continents in the mid-latitudes. Salinity fluxes contribute positively to the generation of P in the

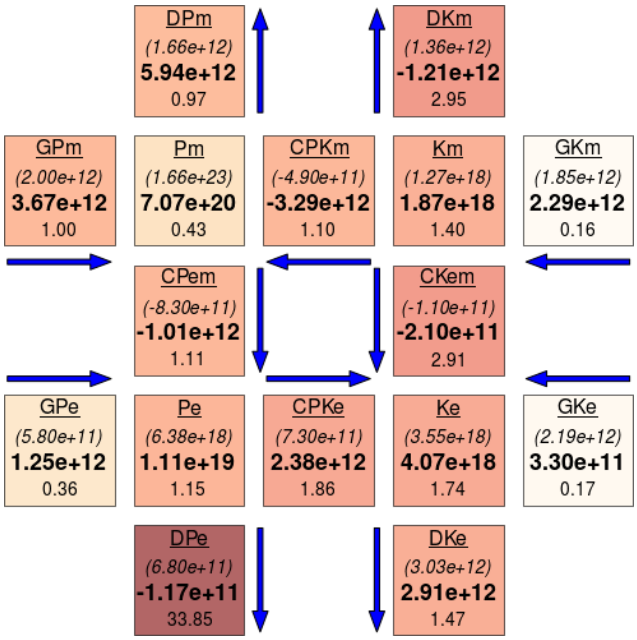

Figure 5: Schematic overview of LEC. The reservoirs are at the junctions (potential (kinetic) energy left (right), mean (eddy) top (bottom)), while their respective generation terms are left and right of them. Between the reservoirs are the conversion terms and above and below the dissipation terms. The large bold number gives the 50 year average size of the energy/power term in J/W, while the italicized number in parentheses above gives the corresponding value of von Storch et al. (2012). The number below indicates the relative variation (standard deviation divided by mean) of the term's time series in percent. The color scale reflects this relative variance.

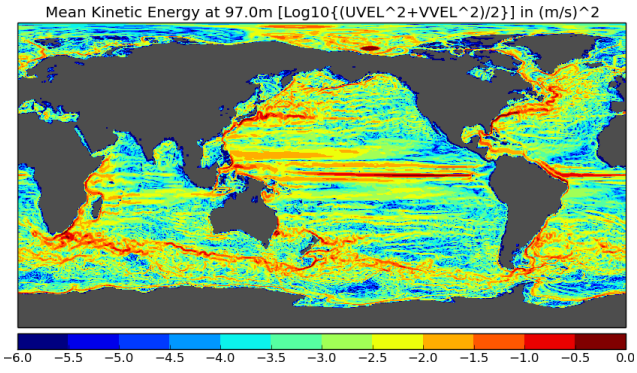

Figure 6: Mean kinetic energy at 97 m depth in the model year 276.

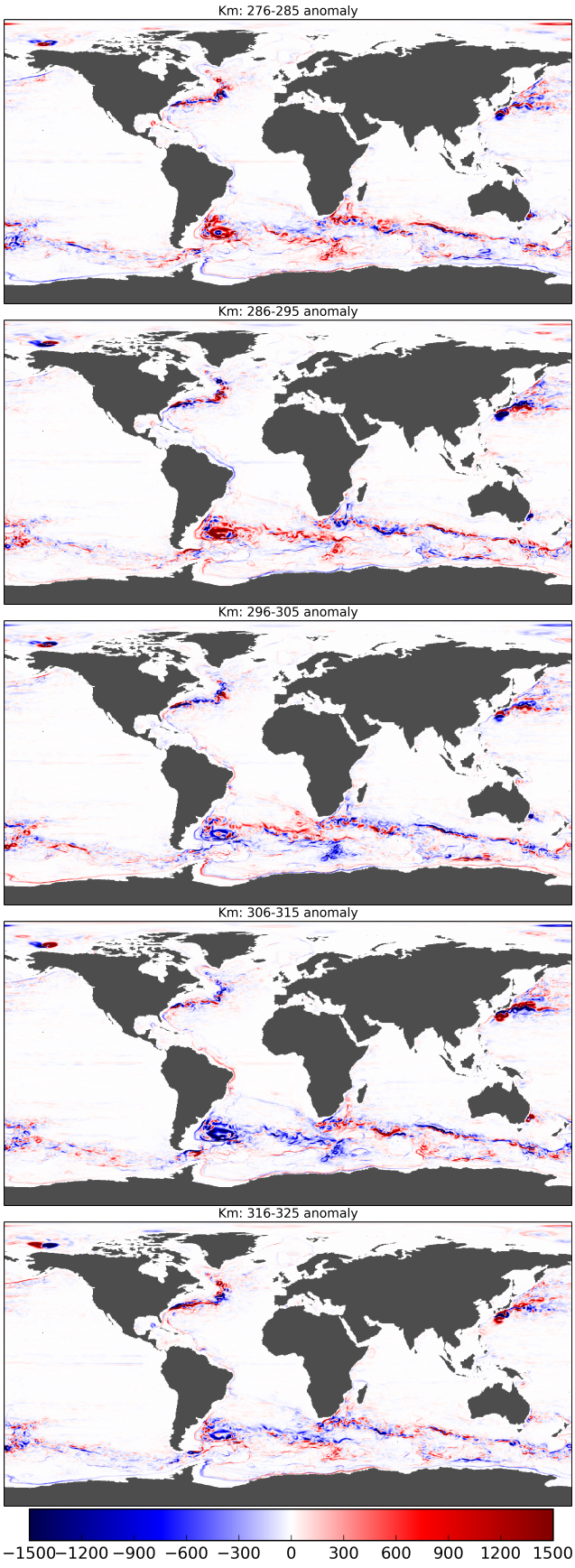

Figure 7: Evolution of the vertically integrated K_m anomalies in the cycle 276-325. The 50 year average is subtracted from the decadal averages. Units are $\mathrm{J\,m^{-2}}$.

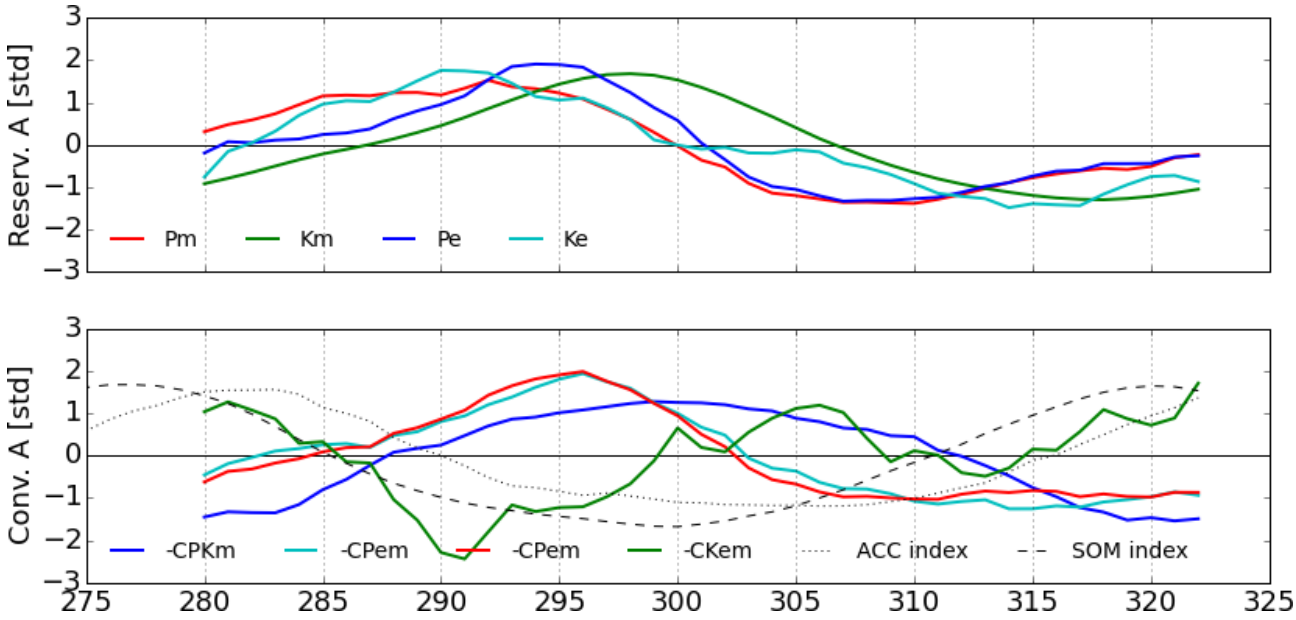

Figure 8: Timing of the reservoir (top) and conversion (bottom) anomalies in region A. The conversion terms are directed in such a way that a positive anomaly indicates a strengthening of the baroclinic pathway. All terms are standardized to have standard deviation 1, their magnitudes can be seen in Table **??**. The SOM and ACC anomaly is also plotted in the lower panel.

tropics and subtropics through evaporation. The generation of kinetic energy predominantly happens in the mid-latitudes with strong storms, particularly in the ACC region. The $G(K_m)$ term is larger than in (von Storch et al., 2012) while the $G(K_e)$ is smaller. This can be explained by the shorter averaging time.

As the conversion between eddy and mean kinetic energy, $C(K_e, K_m)$, is associated with strong currents and their corresponding horizontal shear through the barotropic instability mechanism.

The conversion term between APE and K are associated with sloping isopycnals such as around Antarctica, and steep bathymetric features.

As there is now a time series available, the change in the reservoir sizes can be explicitly calculated and does not have to be set to zero as in the steady state assumption. The dissipation term in equation (9) can then be recalculated:

$$D(X) = \frac{\mathrm{d}X}{\mathrm{d}t} - G(X) - C(Y, X) \tag{11}$$

where $C(Y, X)$ includes both conversion terms to/from the reservoir X. Calculating the time derivatives of the reservoirs, one arrives at numbers that are far smaller than the respective generation and conversion terms (see Table 2).

Table 2: Energy fluxes in GW averaged over 50 years. Changes in reservoirs sizes, $|\mathrm{d}X_x/\mathrm{d}t|$, are much smaller than other fluxes.

	P_m	P_e	K_m	K_e
$\lvert \mathrm{d}X_x/\mathrm{d}t \rvert$	0.02	0.003	0.0007	0.002
$G(X_x)$	3.68	1.25	2.29	0.33
$C(X_y, X_x)$	−1.01	1.01	−0.21	0.21
$C(Y_x, X_x)$	3.29	−2.38	−3.29	2.38
$D(X_x)$	−5.95	0.12	1.21	−2.92

Considering the incomplete physics and assumptions made in the derivation of the LEC terms, the steady state assumption is good in the sense that the errors introduced by it are small.

5.2 extended SOM

The SOM goes through another cycle in the years 376-326 starting in the warm phase, going through a cold phase and ending in a warm phase. Figure 2 shows the context for the the current cycle while Fig. 3 shows the vertically integrated OHC anomaly. The SOM cycle described in Le Bars et al. (2015) can be observed with the same spatial patterns.

The vertical OHC anomaly plots (Fig. 3) have not been detrended while the OHC time series (OHC in Fig. 2/4) are quadratically detrended because

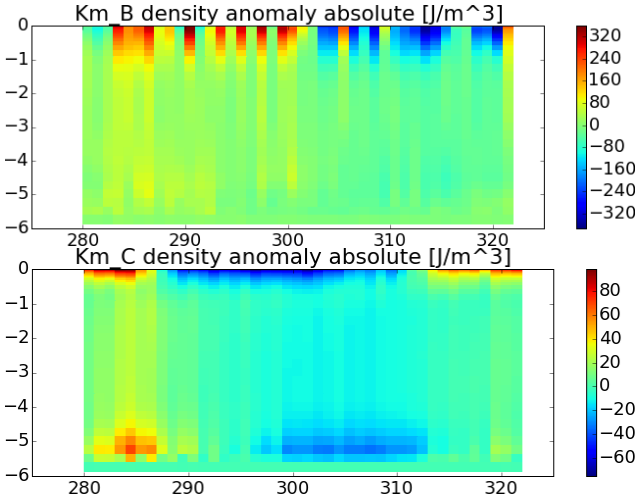

Figure 9: Hovmoeller diagrams of the mean kinetic energy in region B (top) and C (bottom).

there is a negative drift in OHC since initialization (not shown). The detrending was based on the complete available time series (years 75-326) therefore the coefficients of the subtracted trend may be different from the ones used by Le Bars et al. (2015).

5.3 Dynamics in AB vs. CD

The different vertical structures of the anomalies in B as opposed to C seen in the Hovmöller diagrams (Fig. 9) indicate that different dynamic processes play a role. Bottom processes seem to be relatively important in C but not B.

The baroclinic pathway, i.e. the conversion of K_m to K_e through the potential energy reservoirs is the first order energy transfer term globally. This can be seen in Fig. 5 where the three conversion terms correponding to the baroclinic pathway are an order of magnitude larger than the barotropic conversion term $C(K_e, K_m)$.

This dominance of the baroclinic pathway is also the case in the ACC. The barotropic conversion, i.e. directly from K_m to K_e, is much weaker. The baroclinic pathway terms, and how they are timed with respect to the overall SOM, can be seen in Figure 8 for region A. In the beginning of the time series, the pathway intensifies until it reaches a maximum around the year 295. The increase in the reservoir sizes is due to a maximum in the generation terms in the year 280. The barotropic pathway, on the other hand, is not very important as $C(K_e, K_m)$ is small (compare Fig. 5) and out of phase (Fig. 8).

In region CD baroclinic pathways not as important as in region AB. This can be seen from the relative strength of the variation in the kinetic and potential anomaly terms in Figure 10. The total potential energy anomalies are much weaker in the gyre region CD than in the ACC region AB while the total kinetic energy anomalies are about the same size.

It is sensible that different dynamics play a role in the two regions as the dominant balances are different. In the ACC, the wind forcing is balanced by bottom drag, while the Weddel gyre is in Sverdrup balance.

5.4 ACC-gyre interaction

In Figure 7 the spatio-temporal evolution of the mean kinetic energy is shown. There is large scale variation in the Southern Ocean on the same time scale as the OHC anomalies. Three regions appear to be involved in the interaction between the circumpolar current and the gyres North and South of the ACC judging by the anomalous mean kinetic energy. From West to East these are: the Argentine Basin, the Agoulhas retroflection area, and the Kerguelen Plateau.

6 Discussion

The globally integrated values of the LEC found in the POP model compare well with the values from von Storch et al. (2012). Compared to the analysis of von Storch et al. (2012), different forcings were used. For example, river runoff exists and contributes to the generation of APE. Furthermore, a different time averaging period of 1 year instead of 10 years was used. This explains, for example, the discrepancy between the kinetic energy generation terms (see Fig. 5) – a shorter time averaging period implies less momentum is transferred to the eddy component and more to the mean component. Moreover, the kinetic energy generation values calculated here and in von Storch et al. (2012) are higher than the 1 TW estimate of Wunsch (1998).

Ferrari and Wunsch (2009) find that 90% of the kinetic energy is in geostrophic eddies. von Storch et al. (2012) find 75% in K_e, while we find a value of 70%.

There remains a problem with two negative dissipation terms, $D(P_e)$ and $D(K_m)$, which is probably related to the numerical implementation of

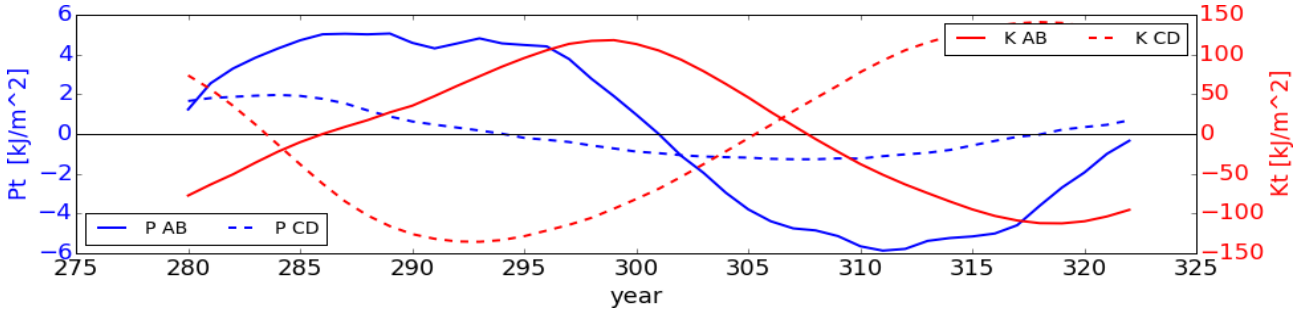

Figure 10: The total potential and kinetic energy anomalies in regions AB and CD.

the calculation of the conversion terms. The use of flux instead of grid point product terms is expected to resolve this problem. All generation and conversion terms have the right sign, however, in the case of P_e and K_m the outgoing conversion terms are stronger than the entering terms requiring the residual dissipation terms to unphysically provide energy. However, the LEC of the total terms (eddy plus mean components) is physically consistent.

When integrating energy terms in regions smaller than the global ocean, energy fluxes across the region's boundaries have to be considered. This has not been included in the above analysis. This is a challenge because there are now two unknowns, fluxes and dissipation, in the energy balance equation. In contrast, the internal energy balance is not affected by this because there is no dissipation of internal energy in the ocean interior.

The OHC signal of the SOM remains a robust feature for the additional cycle the model was run (Fig. 2). All LEC terms show variability on the multidecadal time scale that is larger than the higher frequency variability.

Vertical Hovmöller plots (e.g. Fig. 9) of energy and heat anomalies show mostly a vertically homogeneous behaviour globally and in the SOM regions specifically. This increases the confidence in the vertically integrated anomaly maps as anomalies will then not cancel out vertically.

Furthermore, a difference in relative importance of processes between the the ACC region B and the gyre region C can be seen in Fig. 9. Topography interaction appears relatively more important in C compared to B.

In the spatial analysis of the heat and K_m anomalies (Fig. 3 and 7) the meandering of a current like the ACC can be an influence. This is visible, for example, in the strongly localized anomalies of the ACC in South-West of Australia resulting from a northward meridional shift between the 286-295 and 306-315 anomaly plots (Fig. 7).

In Fig. 7, the overall K_m anomalies in the ACC South of the Atlantic exhibit the same cycle as the ACC transport with a maximum in the decadal average 286-295 and a minimum in 306-315. Furthermore, the Argentine Basin Modes (Weijer et al., 2007) at the confluence of the Malvinas and Brazil Currents are affected and strengthen and weaken with the ACC. This suggests that there is interaction of the mode with subtropical gyres in addition to the ACC-subpolar gyre interaction proposed in Le Bars et al. (2015).

In the vertically integrated K_m plots (Figure 7) three key regions are visible in which the ACC interacts with flow features South of it. These regions are East of the Drake Passage, in the Agoulhas retroflection area and at the Kerguelen Plateau. Based on the different topographic and ocean flow properties of these regions, at least two different mechanisms are suggested.

First, South of Africa, the ACC interacts with Agoulhas retroflection eddies and is perturbed. An increased meridional transport by eddies (Sallée et al., 2008) follows. East of the Drake Passage the ACC similarly interacts with the highly variable modes of the Argentine Basin.

Second, East of the Drake Passage and at the Kerguelen Plateau (50 °S, 70 °E), eddy-topography interaction seems to enhance meridional eddy anomalies. This is plausible as the ACC is a full depth feature resulting from the balance wind forcing and bottom drag (Rintoul et al., 2001). The ACC is subject to topographic steering but meets both at East of the Drake Passage and at the Kerguelen Plateau abrupt topographical changes.

7 Conclusion

For the first time, the time dependency of the LEC has been investigated. Multidecadal variability is observed in all the energy terms; relative variability in the order of percent for the globally integrated values are common.

The SOM time series has been expanded and the SOM seems to be a robust feature. The confidence that the SOM is a mode of internal variability and not an adjustment is increased by the additional cycle that neither grows nor weakens in amplitude.

Different dynamics in ACC and gyre region are observed. The baroclinic pathway of energy transfer is dominant in the circumpolar current region AB while the barotropic conversion is relatively more important in the gyre region BC. This has been shown through the timing of the baroclinic pathway terms in region A and the relative importance of anomalies in the total potential and kinetic energies in region Ab and CD. Aside from baroclinic and barotropic processes, topography interaction seems to play a role as can be seen in the Hovmöller diagrams.

The interaction between several large-scale ocean regimes is observed, including the ACC and subtropical/-polar gyres. Three key regions for the SOM dynamics are identified where the ACC interacts with the polar gyres: East of the Drake Passage, in the Agoulhas retroflection region, and at the Kerguelen Plateau. At the first two, eddy-mean flow interaction must be important, while eddy-topography interaction may be more important in the latter. The Kerguelen region did not stand out in the OHC plots of Le Bars et al. (2015).

However, the exact mechanisms of the SOM remain elusive. Further research is thus suggested. This study started at the complex end with a high resolution, realistic geometry and forcing ocean model to explore the regions and processes involved in a multidecadal variability mode. Minimal models may give insights into essential mechanisms. More understanding can be developed through a more detailed spatial analysis of the terms of the LEC.

The fact, that eddies are crucial in exciting and maintaining the SOM (Le Bars et al., 2015), suggest that more internal variability can be expected in future fully coupled climate model that will contain an eddy-resolving ocean component as opposed to today's relatively low-resolution ocean components (IPCC WGI, 2014).

References

Eden, C., Czeschel, L., and Olbers, D. (2014). Toward Energetically Consistent Ocean Models. *Journal of Physical Oceanography*, 44(12):3160–3184.

England, M. H., McGregor, S., Spence, P., Meehl, G. a., Timmermann, A., Cai, W., Gupta, A. S., McPhaden, M. J., Purich, A., and Santoso, A. (2014). Recent intensification of wind-driven circulation in the Pacific and the ongoing warming hiatus. *Nature Clim. Change*, 4(3):222–227.

Ferrari, R. and Wunsch, C. (2009). Ocean Circulation Kinetic Energy: Reservoirs, Sources, and Sinks. *Annual Review of Fluid Mechanics*, 41(1):253–282.

Hansen, J., Sato, M., Kharecha, P., and von Schuckmann, K. (2011). Earth's energy imbalance and implications. *Atmospheric Chemistry and Physics*, 11(24):13421–13449.

Huang, R. X. (2004). Ocean, Energy flows in. In *Enyclopedia of Energy*, pages 497–509.

IPCC WGI, editor (2014). *Climate Change 2013 - The Physical Science Basis*. Cambridge University Press, Cambridge.

Johnson, G. C. and Parsons, A. R. (2015). Global Oceans. In *State of the Climate in 2014*, number July, chapter 3, pages 59–90.

Kahan, W. (1965). Pracniques: further remarks on reducing truncation errors. *Communications of the ACM*, 8(1):40.

Karl, T. R., Arguez, A., Huang, B., Lawrimore, J. H., McMahon, J. R., Menne, M. J., Peterson, T. C., Vose, R. S., and Zhang, H.-M. (2015). Possible artifacts of data biases in the recent global surface warming hiatus. *Science*, 348(6242):1469–1472.

Kosaka, Y. and Xie, S.-P. (2013). Recent global-warming hiatus tied to equatorial Pacific surface cooling. *Nature*, 501(7467):403–7.

Le Bars, D., Dijkstra, H. A., and Viebahn, J. P. (2015). A Southern Ocean Mode of Multidecadal Variability . *Geophysical Research Letters*, pages 1–21.

Lorenz, E. N. (1955). Available Potential Energy and the Maintenance of the General Circulation. *Tellus A*.

Rintoul, S. R., Hughes, C., and Olbers, D. (2001). The Antarctic Circumpolar Current System. In Siedler, G. and Church, J., editors, *Ocean Circulation and Climate*.

Sallée, J. B., Speer, K., Morrow, R., and Lumpkin, R. (2008). An estimate of Lagrangian eddy statistics and diffusion in the mixed layer of the Southern Ocean. *Journal of Marine Research*, 66(4):441–463.

Sandström, J. W. (1908). Dynamische Versuche mit Meerwasser. *Annalen der Hydrographie und der Maritimen Meteorologie*, 36:6–23.

Schwartz, S. E. (2007). Heat capacity, time constant, and sensitivity of Earth's climate system. *Journal of Geophysical Research: Atmospheres*, 112(24):1–12.

Steinman, B. a., Mann, M. E., and Miller, S. K. (2015). Atlantic and Pacific multidecadal oscillations and Northern Hemisphere temperatures. *Science*, 347(6225):2269–2272.

von Storch, J.-S., Eden, C., Fast, I., Haak, H., Hernández-Deckers, D., Maier-Reimer, E., Marotzke, J., and Stammer, D. (2012). An estimate of Lorenz energy cycle for the world ocean based on the 1/10Â° STORM/NCEP simulation. *Journal of Physical Oceanography*, (1992):120821111920009.

Weijer, W., Vivier, F., Gille, S. T., and Dijkstra, H. A. (2007). Multiple Oscillatory Modes of the Argentine Basin. Part I: Statistical Analysis. *Journal of Physical Oceanography*, 37(12):2855–2868.

Wunsch, C. (1998). The Work Done by the Wind on the Oceanic General Circulation. *Journal of Physical Oceanography*, 28(11):2332–2340.

Wunsch, C. and Ferrari, R. (2004). Vertical Mixing, Energy, and the General Circulation of the Oceans. *Annual Review of Fluid Mechanics*, 36(1):281–314.